Article

Neuron

Hsc70-4 Deforms Membranes to Promote Synaptic Protein Turnover by Endosomal Microautophagy

Highlights

- The Hsc70-4 chaperone can deform membranes
- Hsc70-4-dependent membrane deformation is required for synaptic microautophagy
- Hsc70-4 promotes turnover of numerous synaptic proteins by endosomal microautophagy
- This quality control pathway regulates the efficiency of neurotransmitter release

Authors

Valerie Uytterhoeven, Elsa Lauwers, Ine Maes, ..., Siewert-Jan Marrink, Sebastian Munck, Patrik Verstreken

Correspondence

elsa.lauwers@cme.vib-kuleuven.be (E.L.), patrik.verstreken@cme.vib-kuleuven.be (P.V.)

In Brief

Uytterhoeven, Lauwers, and Maes et al. conducted a proteome-wide screen for membrane-deforming proteins and found the chaperone Hsc70-4. They show that Hsc70-4-dependent membrane deformation promotes endosomal microautophagy at presynaptic terminals, facilitating the degradation of synaptic proteins and promoting neurotransmitter release.

Uytterhoeven et al., 2015, Neuron *88*, 735–748
November 18, 2015
http://dx.doi.org/10.1016/j.neuron.2015.10.012

CellPress

Neuron
Article

Hsc70-4 Deforms Membranes to Promote Synaptic Protein Turnover by Endosomal Microautophagy

Valerie Uytterhoeven,[1,2,5] Elsa Lauwers,[1,2,5,*] Ine Maes,[1,2,5] Katarzyna Miskiewicz,[1,2] Manuel N. Melo,[4] Jef Swerts,[1,2] Sabine Kuenen,[1,2] Rafaël Wittocx,[1,2] Nikky Corthout,[3] Siewert-Jan Marrink,[4] Sebastian Munck,[3] and Patrik Verstreken[1,2,*]
[1]KU Leuven, Center for Human Genetics
[2]VIB Center for the Biology of Disease
Leuven Institute for Neurodegenerative Disease (LIND), Laboratory of Neuronal Communication, Herestraat 49, 3000 Leuven, Belgium
[3]VIB Bio-Imaging Core Facility, Herestraat 49, 3000 Leuven, Belgium
[4]Groningen Biomolecular Sciences and Biotechnology Institute and Zernike Institute for Advanced Materials, University of Groningen, Nijenborgh 7, 9747 AG Groningen, The Netherlands
[5]Co-first author
*Correspondence: elsa.lauwers@cme.vib-kuleuven.be (E.L.), patrik.verstreken@cme.vib-kuleuven.be (P.V.)
http://dx.doi.org/10.1016/j.neuron.2015.10.012

SUMMARY

Synapses are often far from their cell bodies and must largely independently cope with dysfunctional proteins resulting from synaptic activity and stress. To identify membrane-associated machines that can engulf synaptic targets destined for degradation, we performed a large-scale in vitro liposome-based screen followed by functional studies. We identified a presynaptically enriched chaperone Hsc70-4 that bends membranes based on its ability to oligomerize. This activity promotes endosomal microautophagy and the turnover of specific synaptic proteins. Loss of microautophagy slows down neurotransmission while gain of microautophagy increases neurotransmission. Interestingly, Sgt, a cochaperone of Hsc70-4, is able to switch the activity of Hsc70-4 from synaptic endosomal microautophagy toward chaperone activity. Hence, Hsc70-4 controls rejuvenation of the synaptic protein pool in a dual way: either by refolding proteins together with Sgt, or by targeting them for degradation by facilitating endosomal microautophagy based on its membrane deforming activity.

INTRODUCTION

Neuronal synapses are specialized communication nodes where presynaptic proteins are used and re-used many times resulting in wear-and-tear, causing their functional decline. To reliably coordinate vesicle trafficking it is crucial to continuously remove dysfunctional components, but at synapses the underlying mechanisms remain elusive. This is an important gap in knowledge as defects in synaptic protein turnover may constitute a basis for neuronal dysfunction in disease (Fernández-Chacón et al., 2004; Nosková et al., 2011; Zhai et al., 2008).

In eukaryotic cells several mechanisms, including chaperone-mediated protein refolding, proteasomal degradation, autophagy and endosomal sorting of transmembrane proteins contribute to the maintenance of a functional protein pool (Bennett et al., 1999; Fernandes et al., 2014; Parzych and Klionsky, 2014; Speese et al., 2003; Uytterhoeven et al., 2011; Yao et al., 2007). As synapses are often located far from the cell bodies, it seems likely they use specialized mechanisms to cope with protein stress.

In cultured mammalian and yeast cells different types of autophagy exist (Parzych and Klionsky, 2014). Macroautophagy is mediated by LC3/Atg8-positive membranes which fuse and completely surround their targets for degradation (Chen and Klionsky, 2011). Similarly, endosomal microautophagy involves the engulfment of proteins by the late endosomal membrane, but in this process proteins are targeted based on a specific protein motif (Dice, 1990; Sahu et al., 2011) that is recognized by the chaperone Hsc70-4 (Horst et al., 1999). In mammalian cells, the same recognition motif also allows Hsc70-4 to target substrates to chaperone mediated autophagy (CMA) where proteins are translocated over the lysosomal membrane through a Lamp2A pore complex (Kaushik and Cuervo, 2012). However, how these degradative pathways are regulated and whether they operate at synapses is elusive.

We reasoned that most autophagic processes involve extensive membrane remodeling. We therefore performed a large scale in vitro membrane deformation screen that is based on the ability of proteins to deform giant unilamellar vesicle (GUV) membranes. If these proteins are mediating protein turnover at synapses, we surmise their deficiency causes electrophysiological defects recordable in e.g., fruit flies. In this screen we identified seven chaperones. One of them, Hsc70-4, is one of the most abundant synaptic proteins (Wilhelm et al., 2014). Hsc70-4 is known to act as a synaptic chaperone (Braell et al., 1984; Morgan et al., 2001; Sharma et al., 2011; Tobaben et al., 2001); but a role for Hsc70-4 in membrane deformation at synapses is not reported.

Here we show that Hsc70-4 deforms membranes in vitro and in vivo in a process that requires the ability of Hsc70-4 to oligomerize. Factors that inhibit oligomerization, ATP and the co-chaperone Sgt, promote Hsc70-4 dependent chaperone activity, suggesting membrane deformation and chaperone activity

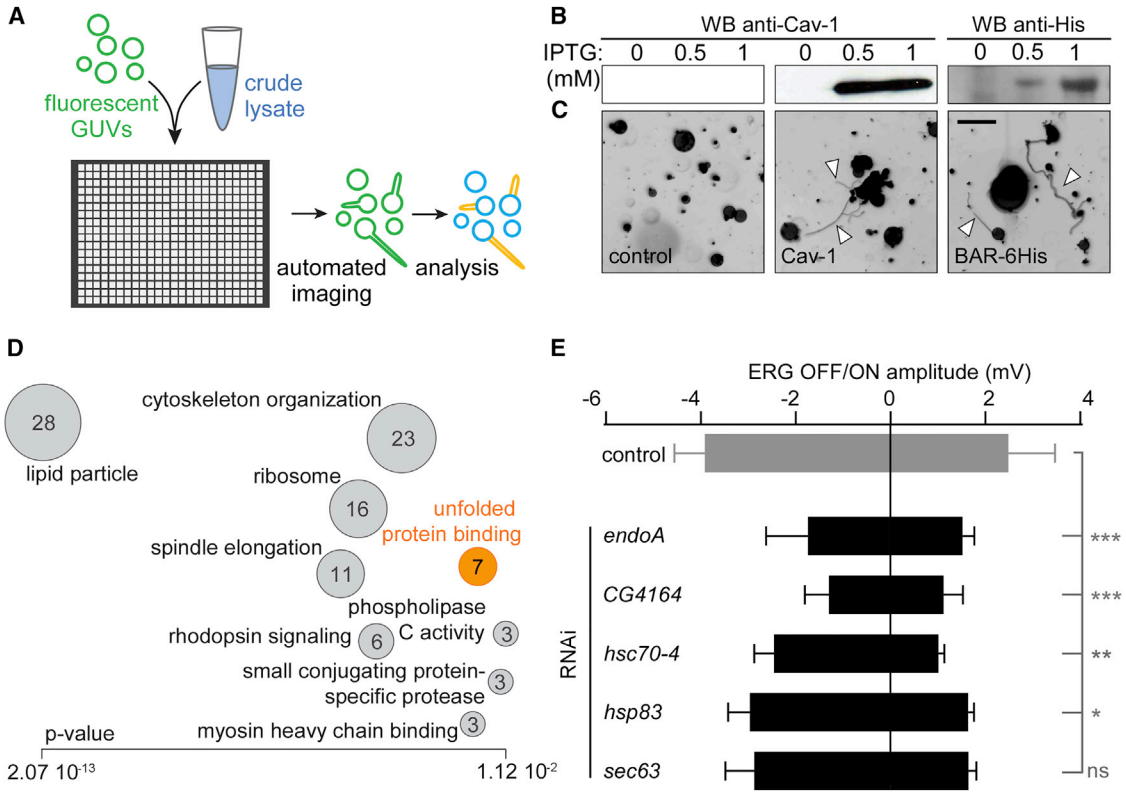

Figure 1. A Membrane Remodeling Screen Identifies Seven Chaperones

(A) Overview of the GUV tubulation screening procedure where crude bacterial lysates are incubated with fluorescent GUVs in a 384 well plate and imaged with an automated microscope. An image analysis algorithm detects GUVs (in blue) and emanating tubules (in orange).

(B) Western blot analysis of crude bacterial lysates showing the presence of human Caveolin-1 (left panel) or the *Drosophila* BAR domain of EndophilinA (right panel, concentrations are indicated).

(C) DiO-labeled GUVs imaged after a 30 min incubation with crude bacterial lysate from bacteria transformed with an empty vector (left panel) or lysate from bacteria expressing human Caveolin-1 (middle panel) or the BAR domain of *Drosophila* EndophilinA (right panel). Arrowheads point at tubules. Scale bar, 50 μm. Fluorescence images are shown with inverted intensities.

(D) Gene ontology enrichment analysis of the 204 positive candidate proteins, performed using DAVID 6.7, showing significant enrichment for several GO terms; the group of chaperones is highlighted.

(E) Quantification of the on and off transient amplitudes of electroretinograms measured in control animals (*GMR-Gal4*) and in animals where *endophilinA* or several of the chaperones we identified in the GUV screen are knocked-down (*GMR-Gal4* > *UAS-RNAi*) (mean ± SEM). Note that RNAi lines to knock down *CG2918*, *hsc70-5*, and *T-cp1* do not exist.

See also Figure S1.

are mutually exclusive activities. Hsc70-4 dependent membrane deformation facilitates endosomal microautophagy at synapses. We show that at fly synapses endosomal microautophagy mediates the turnover of synaptic proteins that harbor an endosomal microautophagy recognition motif and we find that the Hsc70-4 co-chaperone Sgt inhibits synaptic microautophagy. Our work indicates that Hsc70-4 controls rejuvenation of the synaptic protein pool in a dual way: either by refolding proteins together with ATP and Sgt, or by targeting them for degradation by microautophagy.

RESULTS

An Image-Based Screen to Identify Membrane-Deforming Proteins

To identify proteins involved in membrane remodeling we performed an unbiased large scale protein-based screen to identify novel neuronal proteins that can deform lipid bilayers. We combined bacterial lysate from *E. coli* overexpressing a specific protein with fluorescently-labeled giant unilamellar vesicles (GUVs) made from a defined mixture of lipids that roughly mimics synaptic membranes (Doeven et al., 2005; Matta et al., 2012) and then assessed membrane remodeling using an automated fluorescence microscope (Figure 1A). Crude bacterial lysate does not deform DiO-labeled GUV membranes, while lysates containing known membrane deforming proteins leads to tubule formation (Figures 1B and 1C) (Farsad et al., 2001; Matta et al., 2012; Parton and Simons, 2007). We then generated a custom cDNA library from neuron-enriched *Drosophila* tissue (see Figure S1A and Supplemental Experimental Procedures available online), and grew 76,200 individual clones. We imaged GUVs incubated with the lysates from these clones and used a custom-made image analysis algorithm (Figures S1B and S1C; Supplemental

Experimental Procedures). The method results in about 10% false positives (Figure S1C), but all positives were independently retested. We isolated 337 cDNAs corresponding to 232 different proteins that can deform GUV membranes. Given that proteins carrying transmembrane segments are unlikely to properly fold in *E. coli*, we retained 204 proteins (Table S1). These positive clones harbor on average significantly longer stretches of protein-coding cDNA sequence compared to random clones (Figure S1D). In further support of specificity, 31 of the proteins were independently identified at least twice. A total of 98 of the 204 positives are also available in a full-length cDNA library (Yu et al., 2011), and 73 of these 98 proteins tested (74%) also cause GUV tubulation, confirming that also most of the full length proteins in our hit list can deform membranes (Figures S1E–S1G).

Seven Chaperones Deform Membranes

Several of the identified proteins are already known to bind and/or deform membranes (e.g., Dynamin, α-SNAP, AP-1-2β, Bap, Spir, Yp1, and Yp2 lipases) (Butterworth et al., 1992; Camidge and Pearse, 1994; Kerkhoff et al., 2001; Sweitzer and Hinshaw, 1998; Winter et al., 2009), but the majority of them have not been connected before to such a function. Gene ontology analysis of the 204 positive hits reveals a very strong enrichment for proteins associated with lipid particles (28 proteins, p value = 2.07×10^{-13}, Figure 1D) (Huang et al., 2009), and 11 proteins are known or predicted to be involved in lipid metabolism (Table S1). Interestingly, our analysis also shows enrichment for unfolded protein binding (seven proteins, p value = 0.00251, Figures 1D and S1G–S1I), suggesting a connection between chaperone-mediated protein homeostasis and membrane remodeling. These seven chaperones are all expressed in the fly brain (FlyAtlas and BrainGenes) and when knocked down specifically in the optic lobe of *Drosophila*, loss of function of *hsc70-4*, *hsp83*, and *CG1416* impairs synaptic transmission in the fly eye based on electroretinogram recordings (Figure 1E) (Pak, 1995), indicating a function for these genes in the control of neuronal communication. One of these chaperones, Hsc70-4 is one of the most abundant synaptic proteins (Wilhelm et al., 2014), and we find that its cochaperones Sgt and CSP are also enriched at synaptic boutons of the *Drosophila* neuromuscular junction (NMJ) (Figure S2A); but a role for Hsc70-4 in membrane deformation is not reported.

Hsc70-4 Deforms Membranes upon Oligomerization

To study the mode of action by which Hsc70-4 deforms membranes, we first asked if the chaperone function of the protein is involved. Given that the chaperone activity of Hsc70-4 requires ATP (Sadis and Hightower, 1992), we conducted GUV membrane tubulation assays in the presence and absence of ATP (Figures 2A and 2B). While in the absence of exogenous ATP, Hsc70-4 extensively tubulates GUV membranes (Figures 2A, 2A′, and 2D), adding ATP inhibits this activity (Figures 2B and 2D), indicating ATP antagonizes Hsc70-4-dependent GUV-tubulation. The cochaperone Sgt (Sharma et al., 2011; Tobaben et al., 2001) promotes the endogenous Hsc70-4 chaperone activity while CSP, another cochaperone, has no effect (see Figures 2H and 2I, below, and Figure S2C). Similar to adding ATP, the addition of Sgt, but not CSP, strongly inhibits Hsc70-4-dependent GUV membrane deformation (Figures 2C, C′, and 2E). Note that Sgt or CSP alone has no effect (Figure 2E). Hence, ATP and Sgt both inhibit Hsc70-4-dependent GUV membrane deformation.

Different mechanisms of membrane deformation are known, including oligomerization of proteins in a lattice at the membrane (Ellis, 2001; Kozlov et al., 2014; Stachowiak et al., 2012). Interestingly, mammalian Hsc70-4 forms oligomers (Angelidis et al., 1999; Benaroudj et al., 1994), and blue native PAGE indicates that fly Hsc70-4 also assembles into oligomeric complexes. The amount of these Hsc70-4 oligomers is reduced when adding ATP (Figure 2F) (Angelidis et al., 1999; Benaroudj et al., 1994). Given that ATP also blocks Hsc70-4 dependent GUV tubulation, the data suggest that oligomeric Hsc70-4 promotes membrane deformation. Further supporting this conclusion we find that addition of purified Sgt also partially depletes Hsc70-4 oligomeric complexes (Figure 2F). Hence, ATP and Sgt are factors that promote Hsc70-4 chaperone activity while inhibiting Hsc70-4 oligomerization and membrane deformation. The data also indicate that the ability of Hsc70-4 to oligomerize is required for membrane deformation.

Hsc70-4's Chaperone Activity and Membrane Deformation Activity Can Be Separated

To provide further evidence that the chaperone function and the membrane deformation function of Hsc70-4 are separable, we created different Hsc70-4 mutants and assessed chaperone activity and GUV membrane deformation (Figures 2G and S2B). In contrast to wild-type Hsc70-4 and Sgt that stimulate the refolding of denatured luciferase (Figures 2H and 2I), Hsc70-4 lacking the C-terminal domain required for Sgt binding (Hsc70-$4^{\Delta CTD}$) or lacking both the substrate binding and C-terminal domains (Hsc70-4^{ATPase}) fails to refold luciferase. Also an ATPase dead Hsc70-4 mutant (Hsc70-4^{D10N}) (Huang et al., 1993) does not refold luciferase in the presence of Sgt and CSP (Figures 2G and 2I). Of note, Hsc70-4^{D10N} is still capable of binding to Sgt (Figures S2D and S2E), indicating that here the lack of refolding activity is not because of a failure to bind its cochaperone.

Next, we tested the ability of the Hsc70-4 mutant proteins to tubulate GUVs. Hsc70-4 mutants that lack a part of the membrane deformation domain identified in our screen (Figure 2G, black line) do not support GUV tubulation (Figures 2J and 2K). Conversely, the ATPase mutant Hsc70-4^{D10N} efficiently deforms GUV membranes similar to wild-type Hsc70-4 (Figures 2J and 2K), indicating the chaperone activity is not required for membrane deformation.

We then investigated if the Hsc70-4-membrane deformation activity affects chaperone activity. The C-terminal domain of Hsc70-4 harbors evolutionary conserved lysines and arginines (Figures S2F and S2G) that interact with negatively charged membranes (Sahu et al., 2011), and we mutated three lysines (K531, K533, and K539) to alanines. The mutant Hsc70-4^{3KA} folds properly, because it binds Sgt (Figures S2D and S2E), and it harbors Sgt-induced luciferase refolding activity (Figure 2I′). However, Hsc70-4^{3KA} fails to deform GUV membranes (Figures 2J and 2K). Hence, the chaperone and membrane deforming activities of Hsc70-4 can be functionally uncoupled.

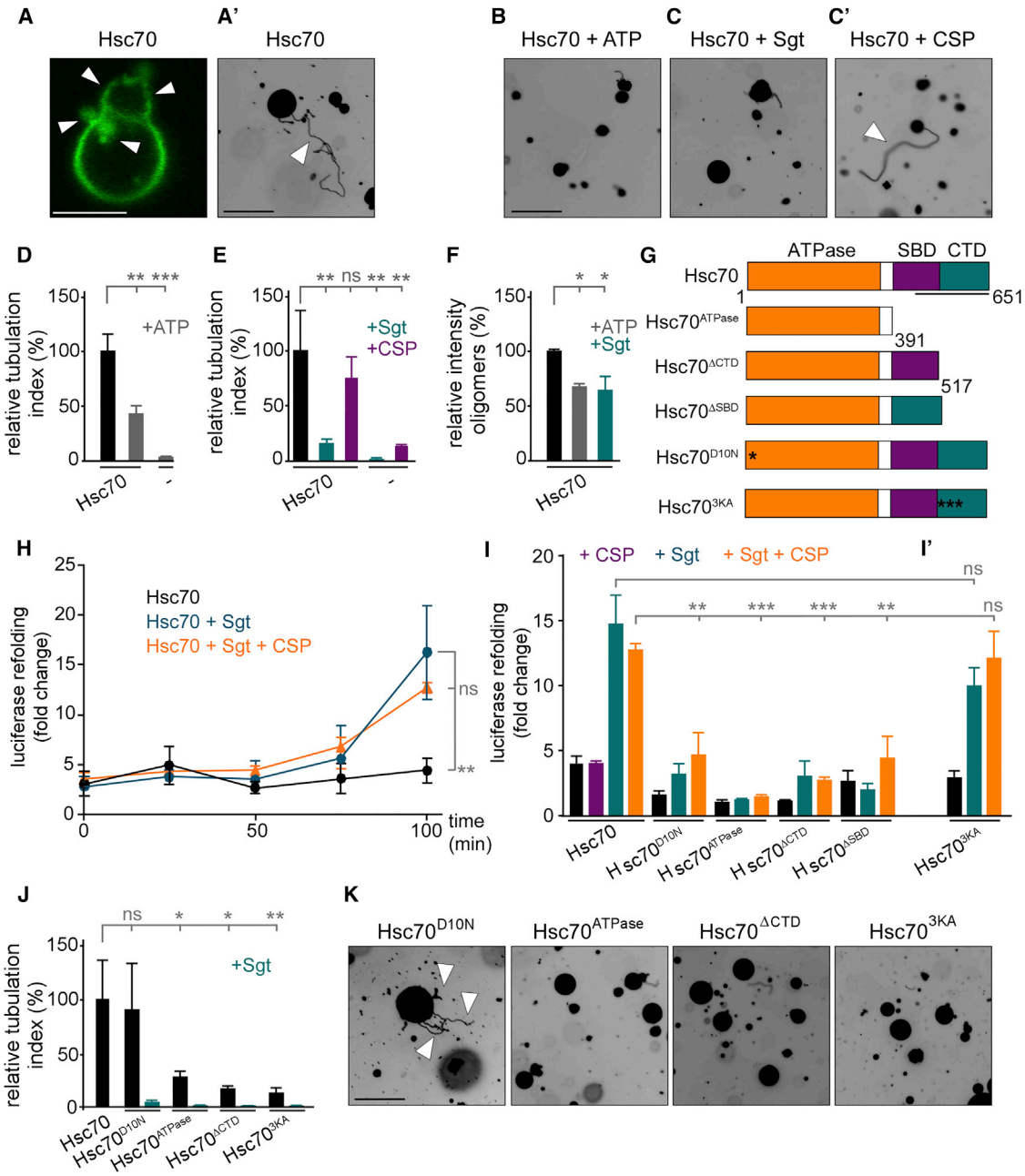

Figure 2. Sgt Inversely Regulates the Membrane Remodeling and the Protein Refolding Activities of Hsc70-4

(A–E) Confocal (A) and fluorescent images (A′–C′) and quantification (D and E) of GUV tubulation assays using purified wild-type Hsc70-4 with or without 10mM ATP (D) or 4 μM Sgt (E). The tubulation index is the total tubule length in μm multiplied by the proportion of GUVs showing tubules. Scale bar, 10 μm for (A) and 50 μm for (A′)–(C′). Arrowheads, tubules.

(F) Quantification of oligomer intensity on western blot after blue native PAGE using bacterial lysate containing wild-type Hsc70-4 with or without 10 mM ATP or 4 μM purified Sgt.

(G) Schematic representation of wild-type and mutant Hsc70-4 proteins. The black bar below Hsc70-4 represents the fragment that was identified in the GUV tubulation screen.

(H) Capacity of Hsc70-4 to refold denatured luciferase over time, expressed in fold change between the refolding in the presence of the chaperone and with buffer alone.

(I and I′) Capacity of Hsc70-4 and Hsc70-4 mutants to refold denatured luciferase with or without CSP and/or Sgt, quantified following a 100 min incubation period.

(J and K) Fluorescent images (K) and quantification (J) of GUV tubulation assays using bacterial lysate containing wild-type or mutant Hsc70-4 or in combination with Sgt-containing lysate. Scale bar, 50 μm. Arrowheads, tubules. All graphs show mean ± SEM.

See also Figure S2.

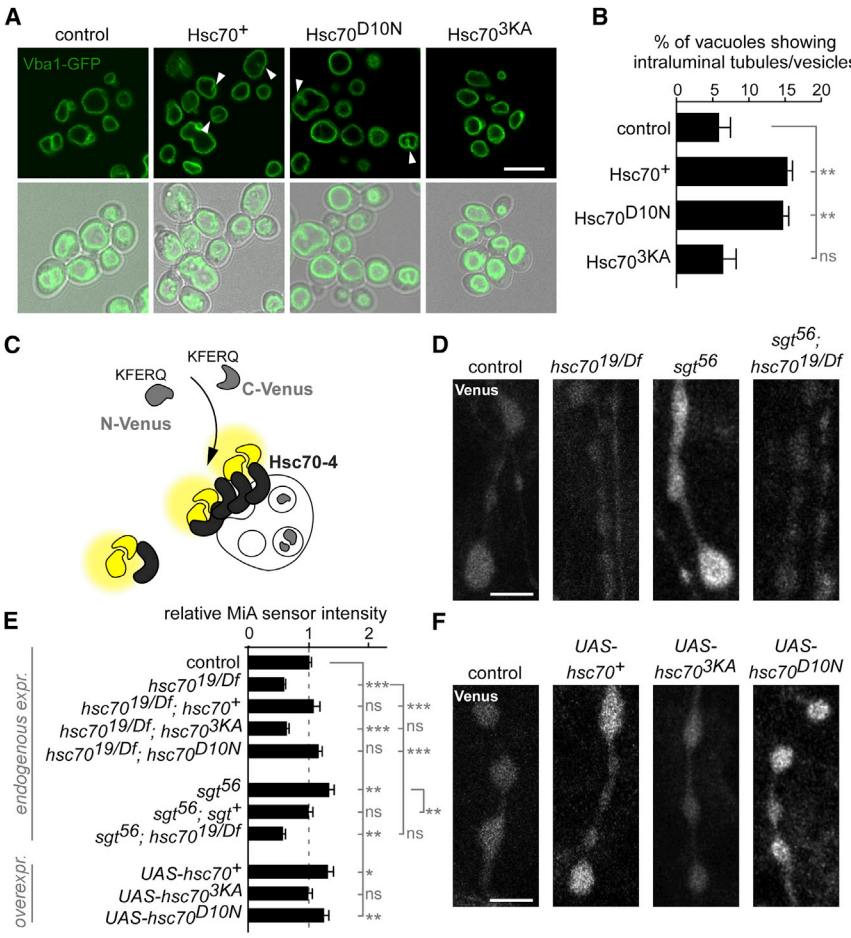

Figure 3. The Membrane Deformation Activity of Hsc70-4 Stimulates Microautophagy at Larval NMJ Terminals

(A and B) Images (A) and quantification (B) of intravacuolar tubules/vesicles of yeast cells expressing the vacuolar marker Vba1-GFP and wild-type or mutant fly Hsc70-4. Arrowheads, intraluminal tubules and vesicles (mean ± SEM).

(C) Schematic representation of the MiA-marker, consisting of both the N- and C-terminal portion of Venus fused to a microautophagy recognition motif (KFERQ). Yellow indicates fluorescence.

(D–F) Representative images of MiA-marker (*elav-Gal4/+; UAS-KFERQ-N-Venus, UAS-KFERQ-C-Venus*) fluorescence expressed at the larval NMJs of controls (*elav-Gal4/+*), *hsc70-4*$^{19/Df}$, *sgt*^{56}, *sgt*^{56}*; hsc70-4*$^{19/Df}$ and of animals harboring endogenous or UAS-overexpression constructs for wild-type and mutant versions of *hsc70-4* (D and F) and quantification of boutonic fluorescence (E) normalized to control values (mean ± SEM). Scale bars, 5 μm.

See also Figure S3.

Moreover, the membrane deforming activity of Hsc70-4 requires oligomerization and membrane association and the factors that promote chaperone activity (ATP and Sgt) simultaneously inhibit the ability of Hsc70-4 to deform membranes.

Hsc70-4 Deforms Membranes In Vivo

To test if Hsc70-4 promotes membrane deformation in vivo we expressed wild-type and mutant Hsc70-4 in *S. cerevisiae* and assessed vacuolar membrane invagination and intraluminal vesicle formation by following Vba1-GFP (Shimazu et al., 2005). We find that expression of wild-type Hsc70-4^{+} results in a clear increase in intraluminal vacuolar tubules and vesicles (Figures 3A and 3B). This effect is lost when expressing Hsc70-4^{3KA} but is retained when expressing Hsc70-4^{D10N} (Figures 3A and 3B). Hence, the membrane deforming activity but not the chaperone activity of Hsc70-4 is sufficient for yeast vacuolar membrane invagination.

Hsc70-4-Dependent Membrane Deformation Stimulates Synaptic Microautophagy

In cultured cells Hsc70-4 has been implicated in targeting proteins with a specific recognition motif to chaperone-mediated autophagy (CMA) and to endosomal microautophagy. Endosomal microautophagy requires deformation of the endosomal membrane (Dice, 1990; Sahu et al., 2011). In mammalian cells, proteins are targeted to CMA and to microautophagy based on the same protein recognition motif. However, in flies CMA is not likely to occur, because Lamp2a, a protein required for this process, is mammalian and avian-specific. In addition, the closest fly homolog, Lamp1, does not harbor the amino acids that in Lamp2a are necessary for CMA (Figure S3A, blue and orange) (Cuervo and Dice, 2000) and finally, fly Hsc70-4 fails to bind to Lamp1 based on coimmunoprecipitations (Figure S3B).

We next tested if Hsc70-4 is involved in promoting endosomal microautophagy at synapses. Few tools to detect this process exist and endosomal microautophagy has not been studied at synapses before. We therefore generated a transgenic sensor that we assessed at synapses. We fused a microautophagy recognition motif, KFERQ (Sahu et al., 2011), to the N- as well as to the C-terminal portion of Venus and expressed both proteins in neurons (*elav-Gal4*; Figure 3C). The idea here is that functional fluorescent protein forms when both moieties concentrate upon targeting for microautophagy. While expression of N- or C- Venus separately does not yield signal (data not shown), when expressed together we observe labeling at synaptic boutons of control animals (Figures 3D–3F). In *hsc70-4* mutants, the fluorescence intensity is lower compared to controls and this defect is rescued by a genomic construct that allows for endogenous re-expression of Hsc70-4^{+}. Expression of the membrane deformation dead mutant Hsc70-4^{3KA} at endogenous levels in *hsc70-4 null* mutants does not rescue the reduced microautophagy sensor fluorescence levels, while re-expression of Hsc70-4^{D10N}, the chaperone dead mutant, restores normal levels of fluorescence (Figure 3E). Note that all genomic constructs result in Hsc70-4 protein that is present at synaptic

boutons (Figure S3C). In addition, the differences in microautophagy sensor fluorescence levels that we report are not because of alterations in sensor expression levels as gauged by quantitative RT-PCR (data not shown). These findings suggest that the membrane deformation capacity of Hsc70-4 is necessary to induce microautophagy sensor signal at the synapse.

To determine if Hsc70-4 is also sufficient to induce microautophagy sensor fluorescence, we overexpressed Hsc70-4^{+}. This condition results in increased microautophagy sensor levels. Interestingly, while overexpression of Hsc70-4^{D10N} also results in increased microautophagy sensor fluorescence, overexpression of Hsc70-4^{3KA} does not (Figures 3E and 3F). The differences in sensor levels we observe are not because of an inability of the overexpressed Hsc70-4 proteins to localize to synapses (Figure S3F) and also not because of differences in sensor expression levels as assessed using quantitative RT-PCR (data not shown). In addition, the sensor is specific to the conditions we tested because the fluorescence levels of an unrelated Split-Venus sensor (PH-GRIP1) that measures PI(3,4,5)P_3 (Khuong et al., 2013) are not different under these conditions (Figures S3D and S3E). Taken together, the data indicate that Hsc70-4 membrane deformation activity is sufficient to induce microautophagy sensor fluorescence.

Providing further evidence for this conclusion we also created *sgt* mutants (Figures S3G–S3I). In *sgt* null mutants we find significantly more microautophagy sensor fluorescence and this increase is dependent on Hsc70-4 because *sgt; hsc70-4* double mutants show the same low fluorescence as seen in *hsc70-4* single mutants (Figures 3D and 3E). Thus, the data indicate that Sgt, a protein blocking Hsc70-4-dependent membrane deformation in vitro, is a negative regulator of Hsc70-4-dependent induction of microautophagy sensor induction at synapses.

To assess if Hsc70-4 harbors pleitrophic effects on alternative protein turnover pathways we assessed if macroautophagy, vesicle endocytosis and proteasomal function are affected in *hsc70-4* mutants and upon expression of wild-type and mutant Hsc70-4. We measured the levels of LC3/Atg8-mCherry, a macroautophagosomal marker (Chang and Neufeld, 2009), we conducted FM1-43 uptake experiments to assess synaptic vesicle endocytosis (Verstreken et al., 2008) and we measured the fluorescence intensity of CL1-GFP, a proteasomal activity marker (Pandey et al., 2007). Under none of the conditions tested do we observe significant changes in these markers (Figures S3J–S3L). Hence, macroautophagy, endocytosis and proteasomal function are not significantly affected by Hsc70-4 under the conditions tested.

Next we used transmission electron microscopy (TEM) to visualize the ultrastructure of synaptic terminals under the conditions where the microautophagy sensor is induced. Many ultrastructural features of boutons in animals overexpressing wild-type and mutant Hsc70-4 and of *sgt* and *hsc70-4* single or double mutants are not different when compared to controls (Figures S4A–S4C). However, we do observe significantly more multivesicular structures with additional intraluminal vesicles in animals overexpressing Hsc70-4^{+} and Hsc70-4^{D10N}, but not in animals overexpressing Hsc70-4^{3KA} (Figures 4E–4H, quantified in Figures 4I and 4J). S*gt* mutants also display more multivesicular structures with an increased number of intraluminal vesicles in comparison to controls (Figures 4A–4D, 4I, and 4J). This defect in *sgt* mutants depends on Hsc70-4, since *sgt; hsc70-4* double mutants show a similarly low number of multivesicular structures and intraluminal vesicles as *hsc70-4$^{19/Df}$* mutants (Figures 4I and 4J). Electron tomograms further highlight the irregular shape of the limiting membranes of these structures, displaying protrusions and invaginations (Figures 4K–4M, arrowheads) that potentially participate in the formation of intraluminal vesicles.

We next hypothesized that some of these multivesicular structures are endosomes containing intraluminal vesicles (ILVs) generated by Hsc70-4-mediated membrane deformation, and if correct, Hsc70-4 should be on their membrane. We used pre-embedding immuno-nano gold TEM with silver enhancement in *sgt* mutants and found Hsc70-4 is much more present on multivesicular structure membranes than in controls (Figures 4N, 4O, S4D, and S4E). These data are consistent with the idea that the multivesicular bodies (MVBs) seen in *sgt* mutants are formed at least in part in an Hsc70-4-dependent manner. These MVBs, which to date are molecularly defined only by the presence of Hsc70-4, are also morphologically distinguishable from classical MVBs since they contain more ILVs per MVB area than MVBs from control animals (Figure 4J).

Synaptic Protein Levels Are Regulated Based on the Presence of a Microautophagy Recognition Motif

We evaluated the importance of microautophagy for global synaptic protein turnover. 53% of 170 synaptic proteins (Lloyd et al., 2000; Wilhelm et al., 2014) harbor at least one microautophagy recognition motif (Figure 5A; Table S2) (Dice, 1990). In both *hsc70-4* mutants and *sgt* mutants we assessed protein levels of Unc-13, EndoA, WASp and Comt/NSF that all contain a microautophagy recognition motif and of StonedB, Complexin, and α-SNAP that do not (Figures 5A′–5D′). The levels of Unc-13, EndoA, WASp, and Comt/NSF are all increased at synaptic boutons of *hsc70-4* mutants, a defect rescued by re-expression of Hsc70-4^{+}, while the levels of StonedB, Complexin, and α-SNAP are not affected (Figures 5B, 5C, 5C′, S5A, and S5B). Conversely, in s*gt* mutants the levels of Unc-13, EndoA, WASp, and Comt/NSF are decreased, a defect rescued by re-expression of Sgt^{+} from a genomic construct. Again, the levels of StonedB, Complexin, and α-SNAP are not affected (Figures 5D, 5D′, S5C, and S5D). This defect in *sgt* mutants depends on Hsc70-4 because in *sgt; hsc70-4* double mutants, the levels of the 4 synaptic proteins are again increased (Figures 5E and E′). These data suggest that Hsc70-4 promotes turnover of synaptic microautophagy recognition motif-containing proteins and that Sgt is a negative regulator.

We next overexpressed Hsc70-4^{+} and Hsc70-4^{D10N} and find decreased levels of Unc-13, EndoA, WASp, and Comt/NSF, while at synapses overexpressing Hsc70-4^{3KA} the levels of these proteins remain unchanged (Figures 5F–5H and 5F′–5H′). Hence, Hsc70-4-dependent membrane deformation promotes the turnover of synaptic proteins with a microautophagy recognition motif.

To find independent evidence that the microautophagy recognition motif is required for protein turnover, we mutated the recognition motifs in Comt and expressed the protein from

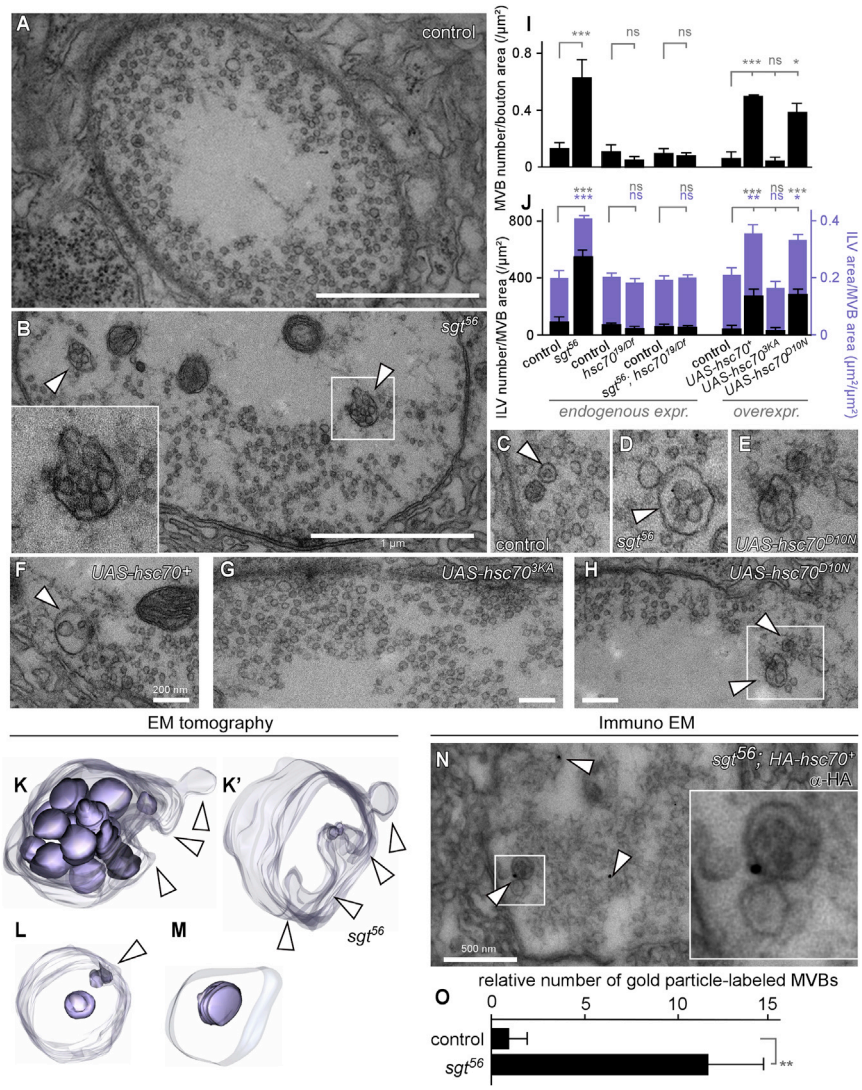

Figure 4. The Membrane Deforming Activity of Hsc70-4 Promotes the Formation of Multivesicular Structures at Larval NMJ Terminals

(A–H) Transmission electron micrographs of NMJ boutons from controls (w^{1118}) (A and C), sgt^{56} mutants (B and D), and animals overexpressing wild-type Hsc70-4 (F) or mutant Hsc70-4 (E, G, and H). White square is inset in (B). Image in (E) is white square in (H). Scale bar in (A) and (B), 1 µm; in (F)–(H), 200 nm. Arrowheads, multivesicular structures.

(I and J) Quantification of the number of multivesicular structures per bouton area (I) and of the number and area of intraluminal vesicles per multivesicular structure area (J) for the same genotypes as in (A)–(H) (mean ± SEM).

(K–M) Electron tomography surface rendering of different types of multivesicular structures in sgt^{56} mutants, showing protrusions and deep invaginations of the limiting membrane (arrowheads).

(N and O) Image (N) and quantification (O) of a pre-embedded immunogold labeled electron micrograph of an NMJ bouton in sgt^{56} mutants harboring an HA-tagged Hsc70-4 transgene (*HA-hsc70-4*$^{+}$) labeled with anti-HA nanogold conjugated antibodies and enhanced using silver staining. (O) Quantification of the relative number of gold particle-labeled MVBs in sgt^{56}; *HA-hsc70-4*$^{+}$/+ mutants compared to controls (*HA-hsc70-4*$^{+}$/+) (mean ± SEM). Arrowheads indicate labeling. White square is right inset that shows a labeled multivesicular structure. Scale bar, 500 nm.

See also Figure S4.

a genomic construct at endogenous levels (Comt^{AA}-Myc). We compared the synaptic levels of Comt^{AA}-Myc (Figure 5I, gray) and wild-type Comt^{+}-Myc (Figures 5F–5H and 5I, dotted lines) in animals expressing wild-type and mutant Hsc70-4. In contrast to Comt^{+}-Myc, we find that the levels of Comt^{AA}-Myc are not reduced upon overexpression of Hsc70-4^{+} or Hsc70-4^{D10N} (Figures 5I and 5I′). As expected, the levels of Comt^{+}-Myc and Comt^{AA}-Myc are both similar upon overexpression of Hsc70-4^{3KA} (Figures 5I and 5I′). These data indicate that the level of Comatose at synaptic boutons is regulated through the microautophagy recognition motifs.

Noticeably, we observed that synaptic transmembrane proteins show less microautophagy recognition motifs in their cytosolic regions than do soluble synaptic proteins (Figure S5E; Table S3). We thus tested if the levels of two transmembrane proteins carrying cytosolic microautophagy recognition motifs, Synaptotagmin1 and syntaxin1A, and one transmembrane protein that does not have such a motif, the vesicular glutamate transporter Vglut (Figure S5F), are affected by sgt or hsc70-4 mutations. We observe no significant difference between the levels of these proteins in the mutants compared to control animals (Figures S5G and S5H). These data suggest that synaptic transmembrane proteins are likely not degraded via microautophagy and rather follow the classical MVB pathway to reach the lysosomal lumen.

Microautophagy Promotes Synaptic Protein Turnover

Given that increasing microautophagy at synapses correlates with decreased levels of synaptic proteins with a recognition motif, we hypothesize that microautophagy turns over proteins more efficiently. The net result of increased turnover would be a younger protein pool. We therefore created transgenic flies that express a fluorescent timer protein fused to Comt/NSF (Comt^{+}-FT). The fluorescent timer slowly converts from blue to red fluorescence emission (Subach et al., 2009) and the red-over-blue ratio reveals the age of the Comt protein pool. Both the blue and red forms of Comt^{+}-FT are detectable in the motor neuron cell bodies and at synapses (Figure 6A). Thus Comt^{+}-FT is transported to NMJs faster than the timer converts from blue to red emission. Comt^{+}-FT also colocalizes with endogenous Comt (Figure 6B) and expression of Comt^{+}-FT rescues the lethality associated with $comt^{clp}$ null mutants, indicating Comt^{+}-FT is

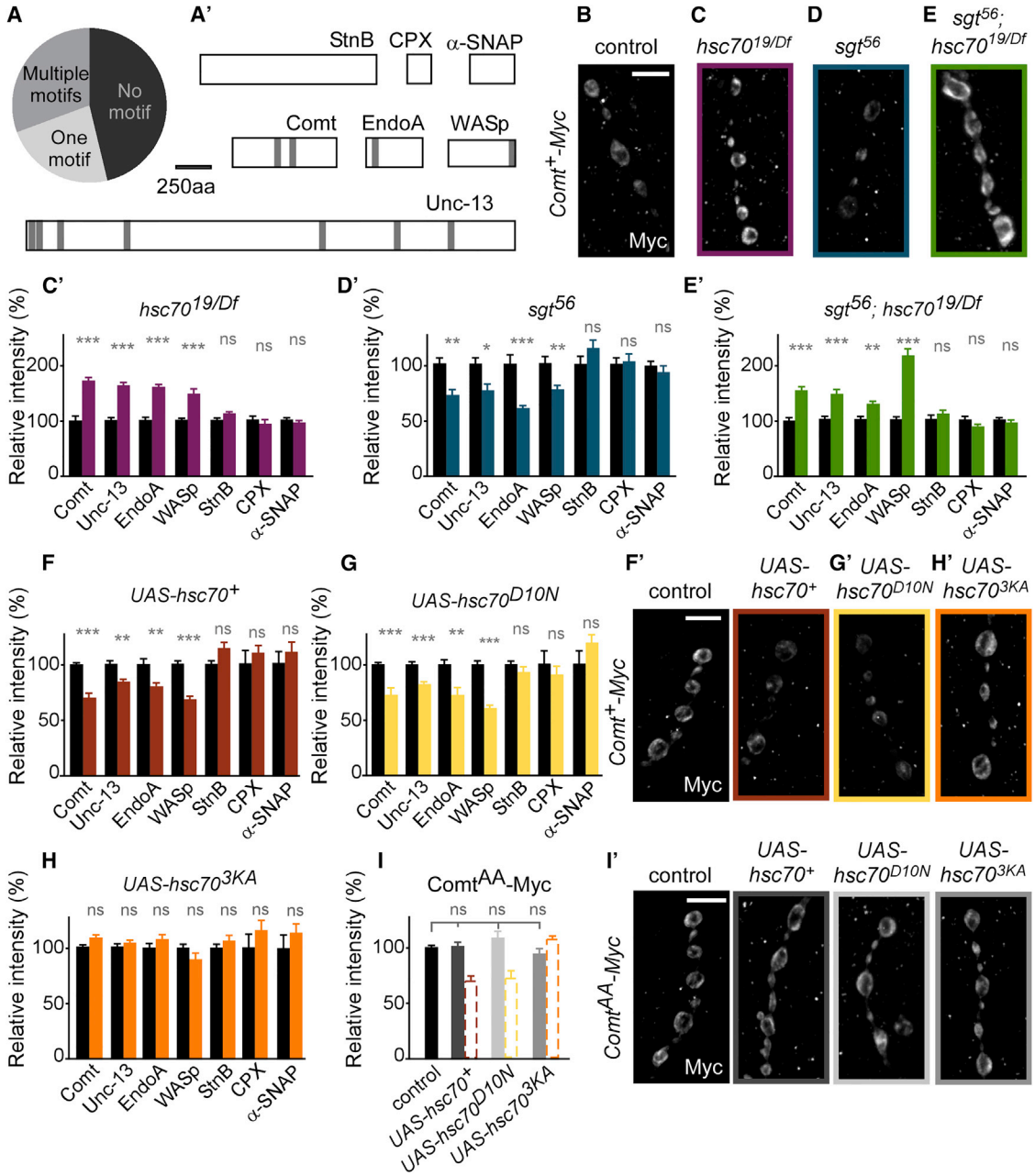

Figure 5. Microautophagy Regulates Synaptic Protein Levels

(A and A′) Percentages of all synaptic proteins with and without a microautophagy recognition motif (A) and examples of synaptic proteins with or without such motifs (A′).

(B–H) Labeling of NMJs of controls (w^{1118}, B), $hsc70^{19/Df}$ (C), sgt^{56} (D), sgt^{56}; $hsc70^{19/Df}$ (E) and of controls for overexpression (*elav-Gal4/+*) (F′) as well as animals overexpressing wild-type and mutant Hsc70-4: *elav-Gal4/+;; UAS-hsc70-4*$^{+}$ (F′), *elav-Gal4/+;; UAS-hsc70-4*^{D10N} (G′) and *elav-Gal4/+;; UAS-hsc70-4*^{3KA} (H′), all with antibodies to detect the synaptic proteins indicated in (A′) using antibodies to Unc-13, EndophilinA, (EndoA), Wiscott-Aldirch Syndrome protein (WASp), StonedB (StnB), Complexin (CPX) and alpha-SNAP (α-SNAP) and using anti-Myc antibodies to detect Comatose (Comt) in animals that express Comt-Myc at endogenous levels (B–E and F′–H′). (C′)–(E′) and (F)–(H) show quantification of labeling intensities of the different markers used in the indicated genotypes.

(I–I′) Images of anti-Myc labeling (I′) and quantification of labeling intensity (I) at NMJs of controls (*elav-Gal4/+*) expressing Comt^{AA}-Myc at endogenous levels, as well as at boutons of animals overexpressing wild-type and mutant Hsc70-4: *elav-Gal4/+;; UAS-hsc70-4*$^{+}$, *elav-Gal4;; UAS-hsc70-4*^{D10N} and *elav-Gal4/+;; UAS-hsc70-4*^{3KA} also expressing Comt^{AA}-Myc. The microautophagy recognition motifs in Comt^{AA}-Myc are both mutated. The dashed bars in I indicate the labeling intensities of Comt-Myc shown in F-H for comparison. Scale bars, 5 μm. All graphs show mean ± SEM.

See also Figure S5.

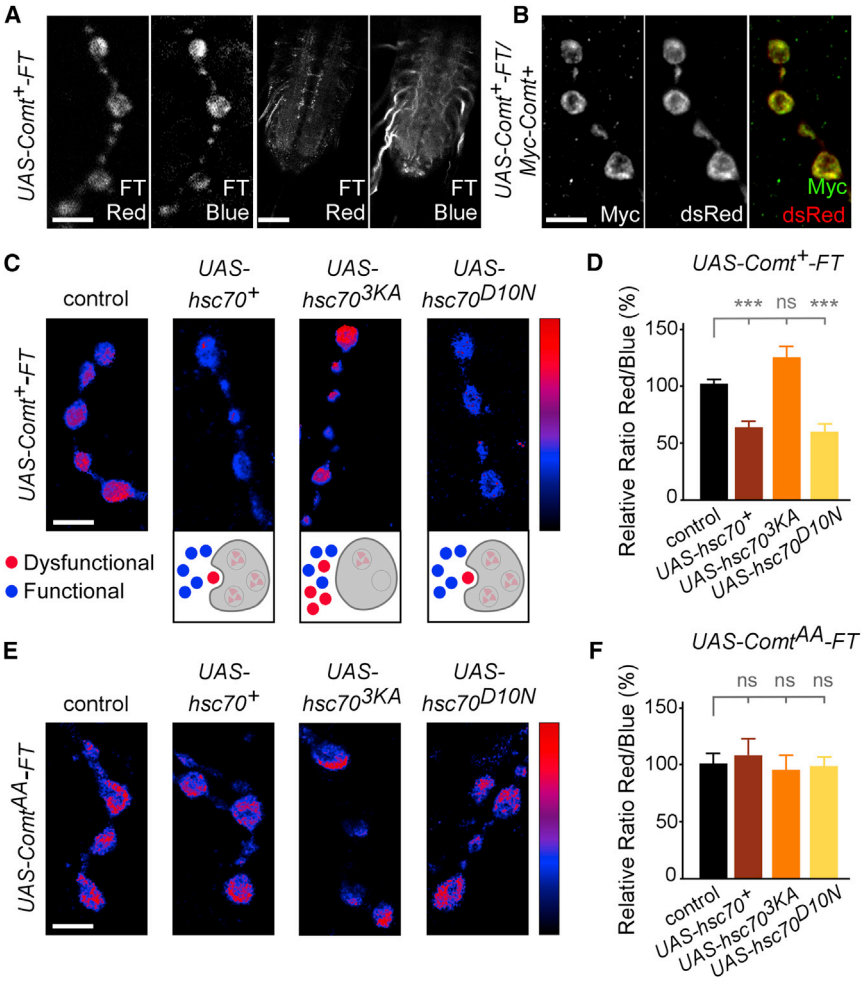

Figure 6. Hsc70-4-Dependent Membrane Deformation Promotes the Turnover of Synaptic Proteins

(A) Red and blue fluorescence at NMJ boutons and the ventral nerve cord of *elav-Gal4; UAS-comt^{+}-FT* that are expressing a Comatose-fluorescent timer fusion protein in all neurons. Scale bar for the 2 left panels, 5 μm; and for the two right panels, 50 μm.

(B) NMJ boutons of *elav-Gal4; UAS-comt^{+}-FT* animals expressing Myc-tagged Comt (*Myc-Comt^{+}*) labeled with anti-dsRed to detect the fluorescent timer protein and anti-Myc to detect endogenously expressed Comt protein. Scale bar, 5 μm.

(C and D) Pseudocolored images (C) and quantification relative to control (D) of red over blue fluorescence intensities of *UAS-comt^{+}-FT* expressed using *elav-Gal4* in control animals (*elav-Gal4; comt^{+}-FT/+*) and in animals expressing wild-type Hsc70-4 and mutant Hsc70-4: *elav-Gal4; UAS-comt^{+}-FT/+; UAS-hsc70^{+}/+*, *elav-Gal4; UAS-comt^{+}-FT/+; UAS-hsc70^{3KA}/+* and *elav-Gal4; UAS-comt^{+}-FT/+; UAS-hsc70^{D10N}/+*. The calibration bar shows red to blue ratio range 1.7–0. Scale bar, 5 μm. The graph shows mean ± SEM.

(E and F) Pseudocolored images (E) and quantification relative to control (F) of red over blue fluorescence intensities of *UAS-comt^{AA}-FT* expressed using *D42-Gal4* in control animals (*comt^{AA}-FT/+; D42-Gal4/+*) and in animals expressing wild-type Hsc70-4 and mutant Hsc70-4: *UAS-comt^{AA}-FT/+; UAS-hsc70^{+}/D42-Gal4*, *UAS-comt^{AA}-FT/+; UAS-hsc70^{3KA}/D42-Gal4* and *UAS-comt^{AA}-FT/+; UAS-hsc70^{D10N}/D42-Gal4*. Scale bar, 5 μm. The graph shows mean ± SEM.

See also Figure S6.

functional. Overexpression of Hsc70-4^{+} or Hsc70-4^{D10N} results in significantly lower Comt^{+}-FT red-over-blue fluorescence ratios compared to controls (Figures 6C and 6D). In comparison, overexpression of the membrane deformation mutant Hsc70-4^{3KA} does not show this phenotype (Figures 6C and 6D). The turnover of Comt^{+}-FT is regulated by the microautophagy recognition motifs because when these sites are mutated, fluorescence ratios of Comt^{AA}-FT are similar in all conditions (Figures 6E and 6F). This result also indicates that expression of Hsc70-4 does not affect the expression levels of the timer constructs. Our notion is further substantiated by the similar levels of blue fluorescence at the synapse in all the conditions we tested (Figure S6). Hence, the membrane deforming activity Hsc70-4 promotes turnover of synaptic Comt protein based on its microautophagy recognition motifs, leading to a younger Comt protein pool.

The Membrane Deformation Activity of Hsc70-4 Promotes Neurotransmitter Release

To assess a role of microautophagy in synaptic transmission we measured neurotransmitter release using two-electrode voltage clamp at NMJs. Loss of *hsc70-4* results in lower microautophagy sensor fluorescence and we also find a lower mean excitatory junctional current (EJC) amplitude compared to controls. This defect is rescued by wild-type Hsc70-4^{+} expressed at endogenous levels. *hsc70-4* null mutants with a genomic *hsc70-4^{3KA}* construct showed reduced microautophagy sensor fluorescence (see Figure 3) and the EJC amplitude in such animals is also not rescued (Figures 7A and 7B), indicating that Hsc70-4-dependent membrane deformation is needed to maintain normal levels of neurotransmitter release. Finally, *hsc-70-4* mutants that harbor a genomic *hsc70-4^{D10N}* construct showed normal levels of microautophagy sensor fluorescence (see Figure 3), but the EJC amplitude is not rescued (Figures 7A and 7B). Hence, the membrane deformation and chaperone activities of Hsc70-4 are each necessary to maintain normal levels of synaptic transmission.

Sgt binds Hsc70-4, promoting chaperone activity and mutants show increased microautophagy sensor fluorescence. In *sgt* mutants we found a dramatic increase in neurotransmitter release compared to controls and this defect was rescued by endogenous expression of Sgt^{+} (Figures 7A and 7B). The increased release is dependent on Hsc70-4 because *sgt; hsc70-4* double mutants show the same low EJC amplitude as *hsc70-4* mutants (Figures 7A and 7B). These data suggest that in the absence of Sgt, Hsc70-4 was liberated to promote

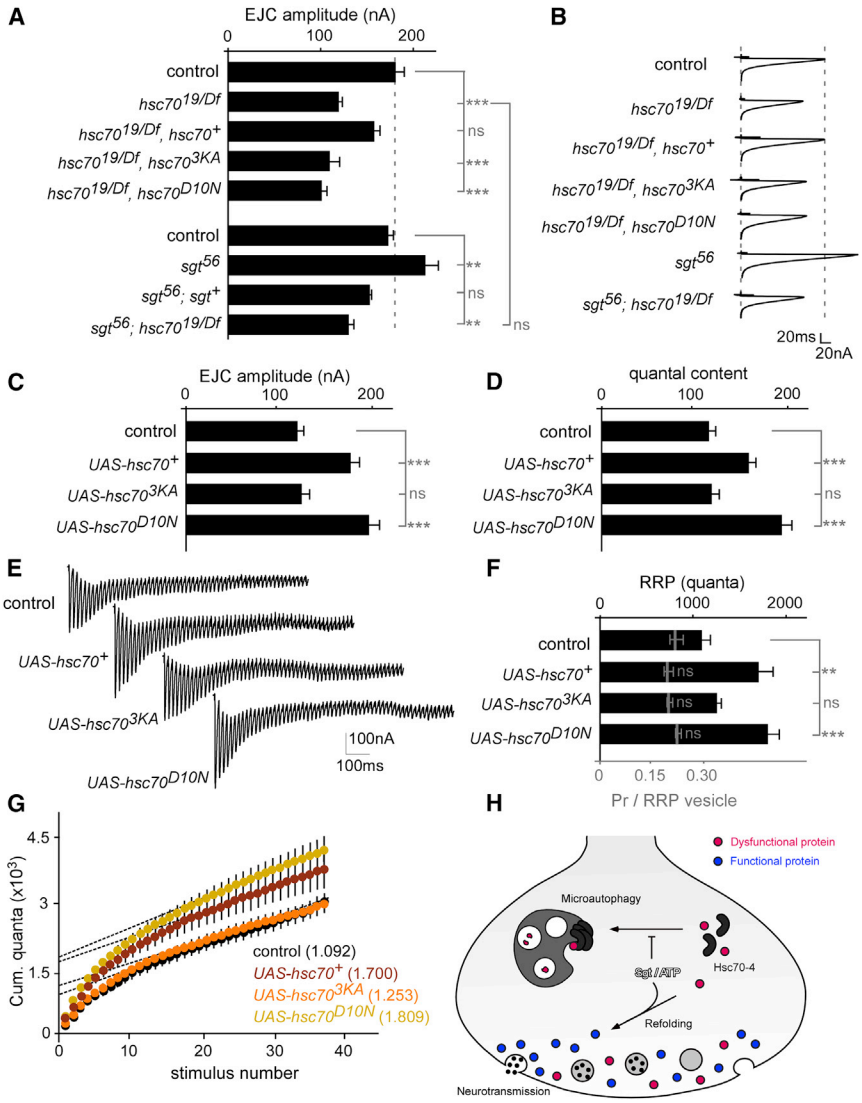

Figure 7. The Membrane Deformation Activity of Hsc70-4 Promotes Neurotransmitter Release and the Formation of a Larger Readily Releasable Pool

(A and B) EJC traces recorded at 0.2 Hz stimulation in 1 mM Ca^{2+} (B) and quantification of the mean EJC amplitude (A) from controls (w^{1118}/+;; *ry*/+), *hsc70-4*$^{19/Df}$ mutants as well as *hsc70-4*$^{19/Df}$, *hsc70-4*$^{+}$/+ or *hsc70-4*$^{19/Df}$, *hsc70-4*^{3KA}/+ or *hsc70-4*$^{19/Df}$, *hsc70-4*^{D10N}/+ mutants that harbor a genomic construct that expresses wild-type or mutant Hsc70-4 at endogenous levels, as well as controls (*yw*), *sgt*^{56} mutants, *sgt*^{56}; *sgt*$^{+}$/+ that express wild-type Sgt at endogenous levels and *sgt*^{56}; *hsc70-4*$^{19/Df}$ double mutants.

(C and D) Quantification of the mean EJC amplitude recorded at 0.2 Hz stimulation in 1 mM Ca^{2+} (C) and quantal content (EJC/mEJC) (D) from controls (*elav-Gal4*/+) and animals overexpressing wild-type and mutant Hsc70-4: *elav-Gal4*/+;; *UAS-hsc70-4*$^{+}$, *elav-Gal4*/+;; *UAS-hsc70-4*^{D10N} and *elav-Gal4*/+;; *UAS-hsc70-4*^{3KA}.

(E–G) EJC traces (E) recorded at 60 Hz stimulation in 5 mM Ca^{2+} and quantification (F) of mean RRP size (in black) from controls (*elav-Gal4*/+) and wild-type and mutant *Hsc70-4*-overexpressing animals during a 60 Hz stimulation train. RRP size is calculated by determining the Y-intercept in cumulative quantal content versus stimulus number graphs (G). (F) Release probability (Pr, in gray) measured in controls (*elav-Gal4*/+) and wild-type and mutant *Hsc70-4*-overexpressing mutants. The Pr is calculated by dividing the quantal content of the initial (first) EJC by the quantal content of the entire RRP.

(H) Model.

All graph show mean ± SEM.

neurotransmitter release, even though under these conditions chaperone function is expected to be present only at basal levels and not stimulated by Sgt.

To further test this idea, we conducted gain of function experiments and overexpressed wild-type and mutant Hsc70-4. Similar to the loss of *sgt*, overexpression of Hsc70-4^{+} results in increased microautophagy sensor fluorescence (see Figure 3) and also increased neurotransmitter release (Figure 7C). In contrast, overexpression of Hsc70-4^{3KA} does not show this increased release. Further indicating specificity, overexpression of Hsc70-4^{D10N} that still harbors membrane deforming activity, again results in increased neurotransmitter release (Figure 7C). Given that the miniature EJC amplitudes are not different between controls and mutants (not shown), the quantal content (EJC/mEJC) upon overexpression of *Hsc70-4*$^{+}$ and *Hsc70-4*^{D10N} is also increased (Figure 7D). Hence, consistent with the results from *sgt* mutants, increased membrane deformation activity, but not increased chaperone activity of Hsc70-4 is sufficient to promote the increased release.

To determine if the observed increase in EJC amplitude in Hsc70-4-overexpressing neurons is due to an underlying increase in the size of the readily releasable vesicle pool (RRP) we stimulated motor neurons at 60 Hz for 600 ms. During the first ~400 ms the vesicles ready for release are depleted, and in the remainder of the stimulation paradigm the low amount of release is sustained by new vesicles refilling the RRP (Habets and Borst, 2007; Uytterhoeven et al., 2011). Compared to controls, we find a larger RRP in animals overexpressing Hsc70-4^{+} or Hsc70-4^{D10N} (Figures 7E–7G). In contrast, animals expressing Hsc70-4^{3KA} show an RRP very similar in size to that measured in controls (Figures 7E–7G). Under these conditions the release probability of a vesicle from the RRP, defined as the quantal content of a single EJC divided by the size of the RRP, is not significantly different (Figure 7F). Hence, the data indicate that the membrane deforming activity of Hsc70-4 facilitates neurotransmitter release by mediating the formation of a larger RRP.

DISCUSSION

This work shows the crucial importance of endosomal microautophagy to keep synapses optimally functional. A previously

unrecognized property of Hsc70-4, its capacity to deform membranes, is necessary and sufficient for endosomal microautophagy at synapses. Although endosomal microautophagy has not been studied at synapses before, our data supports a model where Hsc70-4-dependent endosomal microautophagy captures synaptic proteins with a specific recognition motif and targets them for degradation. We propose that synaptic proteins, modified for instance by oxidation, partial denaturation or other modifications, impede with the release process. Endosomal microautophagy, as demonstrated in this work, promotes turnover thereby rejuvenating the protein pool. Our data suggest that this younger protein pool promotes increased presynaptic efficacy (Figure 7H). Hsc70-4 has a dual function: it can refold target proteins, a process promoted by ATP and its cochaperone Sgt, or it can induce synaptic microautophagy to degrade old proteins. We propose that Hsc70-4 is a central regulator of synaptic robustness and protein homeostasis and our work suggests that this protein is crucial to maintain an active synaptic protein pool.

Hsc70-4 Can Deform Membranes

Many cell biological processes require membrane bending and shaping. We performed an unbiased screen for proteins that can deform membranes. As far as we know, this approach is unique and successful as we identified 204 unique proteins among which 7 chaperones; one of them being Hsc70-4. Hsc70-4 requires two features to deform membranes: (1) the protein needs to oligomerize, and (2) it needs to interact with the membrane. We show that adding ATP or Sgt inhibits oligomerization of Hsc70-4 and at the same time prevents membrane deformation. While inhibiting oligomerization, ATP and Sgt induce Hsc70-4-dependent chaperone activity, indicating that they act as a binary switch to regulate Hsc70-4 activity. Hsc70-4 also harbors three evolutionary conserved positively charged residues in its C-terminal domain that have been shown to interact with the membrane of endosomes (Sahu et al., 2011). We now show that when these three residues are mutated to alanines, Hsc70-4 loses the capacity to deform membranes in vitro and in vivo. Hence, similar to other membrane deforming protein complexes (Farsad et al., 2001; Kozlov et al., 2014; Sweitzer and Hinshaw, 1998), membrane attachment and oligomerization are features needed by Hsc70-4 to deform membranes. An attractive model is that Hsc70-4 together with additional endosome-associated machines such as the ECRTs (Hanson et al., 2008), invaginates the endosomal membrane to create intraluminal vesicles. This idea is further underscored by our finding that the number of multivesicular structures seen by TEM at synapses dramatically increases upon overexpression of wild-type Hsc70-4, but not upon overexpression of Hsc70-4^{3KA}.

Microautophagy Turns Over Synaptic Proteins and Promotes Synaptic Transmission

Synapses are often far from the cell bodies, but the mechanisms by which synaptic proteins are turned over are poorly understood. Our analyses indicate that more than half of the synaptic proteins harbor a KFERQ-motif that targets proteins to chaperone mediated autophagy or to microautophagy. Mutating this motif, as we show in this work, neutralizes the ability of Hsc70-4 to mediate the turnover of these synaptic proteins as well as of our fluorescent timer construct and our Split-Venus microautophagy reporter. We ascribe these changes to defects in endosomal microautophagy-mediated protein degradation as we found that chaperone mediated autophagy is not likely to occur in fruit flies. These findings also promote *Drosophila* as an ideal system to study the role of endosomal microautopahgy in neurons and at synapses without overlapping effects of chaperone mediated autophagy.

The endosomal microautophagy recognition motif may act similar to a PEST sequence that targets proteins for degradation (Rogers et al., 1986): the longer a protein is around, the higher the probability it becomes damaged but also the higher the probability it encounters Hsc70-4 that may target the protein for endosomal microautophagy. Hence the net result of increased microautophagy is a younger protein pool, consistent with our findings using fluorescent timer fusion proteins. Our work indicates that endosomal microautophagy is a mechanism of targeted turnover of synaptic proteins. We propose that damaged older proteins may have a negative impact on synaptic function, due to their inability to undergo the correct sequence of spatially and temporally regulated protein-protein interactions needed for synaptic transmission (Jahn and Fasshauer, 2012). By engaging in dead-end complexes, these proteins would dampen the efficiency of the presynaptic machinery. Interestingly, we show that removing these older proteins from wild-type synapses by endosomal microautophagy facilitates the release process. The consequence of this finding is that our work indicates that under normal wild-type conditions, old and damaged proteins reside at the synapse and they suppress neurotransmitter release. Given that numerous synaptic proteins harbor endosomal microautophagy recognition motifs, endosomal microautophagy under control of Hsc70-4 may prove to not only be a mechanism of synaptic protein turnover, but may also constitute an elegant and local mechanism that regulates synaptic plasticity and synaptic strength. Dysfunction of such a clearance mechanism could have direct relevance for the many age-related neurodegenerative disorders which are in many cases diseases of abnormally folded protein that affect synapses in the early stage of the disorders.

EXPERIMENTAL PROCEDURES

Drosophila Genetics

All fly stocks were kept on standard corn meal and molasses medium at RT. For electrophysiology and immunohistochemistry experiments, *hsc70-4* mutants and controls were grown on black currant plates with fresh yeast. *Gal4-UAS* and control flies were grown at 25°C on standard food. Deficiencies and transgenic stocks were obtained from the Bloomington Stock Center Indiana or from the Vienna *Drosophila* RNAi Centre; or were a gift (*hsc70-4* mutants from Konrad Zinsmaier, University of Arizona; UAS-mCherry-Atg8a from Thomas Neufeld, University of California and UAS-CL1-GFP from Udai Pandey, University of Pensylvania medical center). See Supplemental Experimental Procedures.

Bacteria and Yeast Manipulations

E. coli cells of the strain DH10B (Invitrogen) and of the strain K12 (KRX), Rosetta (DE3) pLysSRARE (Novagen) were grown at 37°C in LB medium with the appropriate antibiotics: 15 μg/ml kanamycin or 100 μg/ml ampicillin

(MP Biomedicals) or 50 μg/ml chloramphenicol (Sigma-Aldrich). Cells of the *S. cerevisiae* strain 23 344c were grown at 30°C in YPD medium (1% yeast extract, 2% bacto peptone, 3% glucose) or in YNB medium without ammonium/amino acids with 10 mM proline, 3% galactose and 0,3% glucose (all reagents from Sigma-Aldrich). Hsc70-4 expression was arrested 2 hr before imaging by adding 3% glucose. Transformation of yeast cells was performed using the standard lithium acetate method.

GUV Tubulation Assay

GUVs were prepared freshly from a mixture of L-α-phosphatidylcholine (PC), L-α-phosphatidylethanolamine (PE), L-α-phosphatidylserine (PS) and cholesterol (chol) 5:2:1:1 (Avanti Polar Lipids) in chloroform (MP Biomedicals):methanol (Merck Millipore) 3:1; by electroformation on ITO-coated glass slides (Visiontek Systems, United Kingdom). Bacterial lysates were incubated with GUVs at room temperature for 30 min before imaging with an automated widefield IN Cell Analyzer 2000 inverted microscope (GE Healthcare) equipped with an S Plan Fluor ELWD 20X objective (corr. collar 0.1-1.3 CFI/60 (0.70 dry)). Tubulation was quantified by measuring the length of all the tubules formed and counting the number of GUVs showing one or more tubules using Image J 1.44o. The total number of GUVs was then determined using an automated image analysis protocol (see Supplemental Experimental Procedures). Finally, a tubulation index was calculated by multiplying the total tubule length in μm by the proportion of GUVs showing tubules. For each condition six images were quantified from three independent tubulation assays. See Supplemental Experimental Procedures.

cDNA Library Generation

Total RNAs were extracted from heads of adult *yw* flies. Reverse transcription was performed with the Superscript III First Strand Synthesis System (Stratagene) using a poly-dT(18) primer. RNAs were then removed by incubating the sample in presence of RNase H (New England Biolabs) and second strand cDNA synthesis was performed by PCR using the Phusion DNA polymerase (New England Biolabs) and a primer comprising a ribosomal binding site (RBS), followed by nine random bases, the last four of which were mixed using the reported base ratio observed upstream from translational start sites (Weir and Rice, 2010) and finally an ATG at the 3′ end (Figure S1A). Double-stranded cDNAs were cloned into the pET-28b-URA3-2μ vector by in vivo recombination in yeast.

Luciferase Refolding Assay

The chaperone activity of Hsc70-4 was measured using QuantiLum Recombinant Luciferase (Promega) essentially as described (Tobaben et al., 2001). See Supplemental Experimental Procedures.

Electrophysiology

ERG and two electrodes voltage clamp recordings were performed as described (Fernandes et al., 2014). See Supplemental Experimental Procedures.

Fluorescence Imaging

Immunohistochemistry was performed as described (Uytterhoeven et al., 2011), except for the fixation of anti-VGlut and anti-Syntaxin, where larval filets were incubated for 5 or 15 min in Bouin's fixative respectively. Blocking medium for anti-Syntaxin contained 0.25% BSA and 5% NGS in 0.4% Triton-PBS. Rabbit anti-Unc-13 1:200 (gift ahead of publication from Stephan Sigrist (Freie Universität Berlin), and the characterization of this reagent will be published elsewhere. Other primary antibodies used were guinea pig anti-EndophilinA pAb 1:1000, rabbit anti-WASp pAb 1:500 (gift from Eyal Schejter, Weizmann Institue of Science), rabbit anti-Stoned B pAB 1:500 (gift from Marie Phillips, University of Melbourne), chicken anti-Myc pAb 1:100 (Bethyl, IMTEC), rabbit anti-Complexin 1:1,000 (gift from Troy Littleton, Massachusetts institute of technology), rabbit anti-α-SNAP 1:1,000 (gift from Leo Pallanck, University of Washington), rabbit anti-dsRed pAb 1:300 (Takara Bio Inc.), mouse anti-DLG pAb 1:500 (DSHB), mouse anti-HA mAb 1:100 (HA.11 clone 16B12, Covance), rat anti-HA mAb 1:500 (Roche), guinea pig anti-Sgt pAb 1:50, mouse anti-CSP mAb (49/92) 1:50, mouse anti-Syntaxin mAb (8C3, DSHB) 1:20, rabbit anti-VGlut pAb (gift from A. Di Antonio) 1:10,000, rabbit anti-Syt1 pAb (DSYT-2, gift from H. Bellen) 1:8,000. Secondary antibodies used were Alexa Fluor 488 or 555 (Invitrogen) or Pacific Blue (Life Technologies) at 1:1,000. The anti-Sgt polyclonal antibody was generated against purified full length Sgt (purification performed as described in Supplemental Experimental Procedures) and injected in guinea pigs (Eurogentec). See Supplemental Experimental Procedures.

Electron Microscopy

TEM, tomography, and data quantification were performed as described (Uytterhoeven et al., 2011). For pre-embedding immune-gold TEM, larval fillets from sgt^{56} mutants and controls w^{1118} both expressing *HA-hsc70-4* were fixed in 4% paraformaldehyde, 0.5% glutaraldehyde in 0,1 M Soerens phosphate buffer (PB, pH 7.4) for 2 hr. In order to quench aldehyde groups, samples were treated with 0.1% $NaBH_4$ diluted in 0.1 M PBS (pH 7.9) for 30 min and washed with PBS (pH 7.4) for 1 hr. Next, tissues were permeabilized with 0.005% Triton X-100 in 0.1 M PBS for 1 hr before blocking the samples with the block solution for goat gold conjugates (Aurion). The primary antibodies anti-HA (HA.11 clone 16B12, Covance) were diluted 1:250 in "incubation" solution containing 0,005% Triton X-100 and 0.1% BSA-c (Aurion) in 0.1 M PBS. Anti-HA antibodies were applied overnight at 4°C, followed by incubation for 6 hr at room temperature. Secondary antibodies (anti-mouse small gold IgG, Aurion) were diluted 1:200 in "incubation" solution and applied overnight. After washing in 0.1 M PB, tissues were post-fixed with 2.5% glutaraldehyde in 0.1 M PB and treated with the silver enhancement kit (Aurion R-GENT SE-EM) at 20°C for 30 min. Tissues were finally processed for EM with a short osmication step in 1% OsO_4 in 0.1 M PB at room temperature for 5 min and contrasting in 2% aqueous solution of uranyl acetate. Tissues were embedded in Durcupan.

Statistical Analysis

Statistical analysis was performed using the appropriate t test or ANOVA model with Dunnett's post hoc test to compare each mean of treatments with the mean of a single control. All data were graphed and statistical analyses were performed using GraphPad Prism 6 (GraphPad Software, La Jolla, California, USA). Error bars indicate SEM. * $p < 0.05$, ** $p < 0.01$, *** $p < 0.001$; ns, not significant.

See also Supplemental Experimental Procedures.

SUPPLEMENTAL INFORMATION

Supplemental Information includes six figures, four tables, and Supplemental Experimental Procedures and can be found with this article at http://dx.doi.org/10.1016/j.neuron.2015.10.012.

AUTHOR CONTRIBUTIONS

V.U., E.L., I.M., and P.V. conceived the study and wrote the paper; V.U., E.L., I.M., K.M., J.S., S.K., R.W., and P.V. conducted experiments and analyzed data; N.C. and S.M. designed algorithms to detect tubules in the screen and provided help with imaging; and S.J.M. and M.N.M. provided valuable insight in the mechanism of Hsc70-4's membrane bending activity.

ACKNOWLEDGMENTS

We thank Sylvain Brohée and Mark Fiers for advice on bioinformatics analyses. We especially thank Stephan Sigrist for sharing his Unc-13 antiserum ahead of publication. We also thank Bruno André, Konrad Zinsmaier, Marie Phillips, Eyal Schejter, Troy Littleton, Leo Pallanck, Hugo Bellen, and Aaron Di Antonio for reagents; and Bart De Strooper, Joris De Wit, Nils Schoovaerts, Elisabeth Rossaert, Bassem Hassan, Giovanni Esposito, Sven Vilain, and other members of the Verstreken laboratory for help, comments, and discussions. Support was provided by a KU Leuven CREA grant (ZKC4633 - CREA/12/023), an ERC Starting Grant (260678), the Research Foundation Flanders (FWO grants G053913N, G079013N and G094915N, postdoctoral fellowship to V.U.), the Hercules Foundation, the Instituut voor Wetenschap en Technologie (IWT grant 111352 to I.M.), the Interuniversity Attraction Pole program by BELSPO,

the research fund KU Leuven, a Methusalem grant of the Flemish government, and VIB.

Received: July 17, 2015
Revised: September 10, 2015
Accepted: September 28, 2015
Published: November 18, 2015

REFERENCES

Angelidis, C.E., Lazaridis, I., and Pagoulatos, G.N. (1999). Aggregation of hsp70 and hsc70 in vivo is distinct and temperature-dependent and their chaperone function is directly related to non-aggregated forms. Eur. J. Biochem. FEBS *259*, 505–512.

Benaroudj, N., Fang, B., Triniolles, F., Ghelis, C., and Ladjimi, M.M. (1994). Overexpression in Escherichia coli, purification and characterization of the molecular chaperone HSC70. Eur. J. Biochem. FEBS *221*, 121–128.

Bennett, M.C., Bishop, J.F., Leng, Y., Chock, P.B., Chase, T.N., and Mouradian, M.M. (1999). Degradation of alpha-synuclein by proteasome. J. Biol. Chem. *274*, 33855–33858.

Braell, W.A., Schlossman, D.M., Schmid, S.L., and Rothman, J.E. (1984). Dissociation of clathrin coats coupled to the hydrolysis of ATP: role of an uncoating ATPase. J. Cell Biol. *99*, 734–741.

Butterworth, F.M., Burde, V.S., and Bownes, M. (1992). Mutant yolk proteins lead to female sterility in Drosophila. Dev. Biol. *154*, 182–194.

Camidge, D.R., and Pearse, B.M. (1994). Cloning of Drosophila beta-adaptin and its localization on expression in mammalian cells. J. Cell Sci. *107*, 709–718.

Chang, Y.Y., and Neufeld, T.P. (2009). An Atg1/Atg13 complex with multiple roles in TOR-mediated autophagy regulation. Mol. Biol. Cell *20*, 2004–2014.

Chen, Y., and Klionsky, D.J. (2011). The regulation of autophagy—unanswered questions. J. Cell Sci. *124*, 161–170.

Cuervo, A.M., and Dice, J.F. (2000). Unique properties of lamp2a compared to other lamp2 isoforms. J. Cell Sci. *113*, 4441–4450.

Dice, J.F. (1990). Peptide sequences that target cytosolic proteins for lysosomal proteolysis. Trends Biochem. Sci. *15*, 305–309.

Doeven, M.K., Folgering, J.H., Krasnikov, V., Geertsma, E.R., van den Bogaart, G., and Poolman, B. (2005). Distribution, lateral mobility and function of membrane proteins incorporated into giant unilamellar vesicles. Biophys. J. *88*, 1134–1142.

Ellis, R.J. (2001). Macromolecular crowding: obvious but underappreciated. Trends Biochem. Sci. *26*, 597–604.

Farsad, K., Ringstad, N., Takei, K., Floyd, S.R., Rose, K., and De Camilli, P. (2001). Generation of high curvature membranes mediated by direct endophilin bilayer interactions. J. Cell Biol. *155*, 193–200.

Fernandes, A.C., Uytterhoeven, V., Kuenen, S., Wang, Y.C., Slabbaert, J.R., Swerts, J., Kasprowicz, J., Aerts, S., and Verstreken, P. (2014). Reduced synaptic vesicle protein degradation at lysosomes curbs TBC1D24/sky-induced neurodegeneration. J. Cell Biol. *207*, 453–462.

Fernández-Chacón, R., Wölfel, M., Nishimune, H., Tabares, L., Schmitz, F., Castellano-Muñoz, M., Rosenmund, C., Montesinos, M.L., Sanes, J.R., Schneggenburger, R., and Südhof, T.C. (2004). The synaptic vesicle protein CSP alpha prevents presynaptic degeneration. Neuron *42*, 237–251.

Habets, R.L., and Borst, J.G. (2007). Dynamics of the readily releasable pool during post-tetanic potentiation in the rat calyx of Held synapse. J. Physiol. *581*, 467–478.

Hanson, P.I., Roth, R., Lin, Y., and Heuser, J.E. (2008). Plasma membrane deformation by circular arrays of ESCRT-III protein filaments. J. Cell Biol. *180*, 389–402.

Horst, M., Knecht, E.C., and Schu, P.V. (1999). Import into and degradation of cytosolic proteins by isolated yeast vacuoles. Mol. Biol. Cell *10*, 2879–2889.

Huang, S.P., Tsai, M.Y., Tzou, Y.M., Wu, W.G., and Wang, C. (1993). Aspartyl residue 10 is essential for ATPase activity of rat hsc70. J. Biol. Chem. *268*, 2063–2068.

Huang, W., Sherman, B.T., and Lempicki, R.A. (2009). Systematic and integrative analysis of large gene lists using DAVID bioinformatics resources. Nat. Protoc. *4*, 44–57.

Jahn, R., and Fasshauer, D. (2012). Molecular machines governing exocytosis of synaptic vesicles. Nature *490*, 201–207.

Kaushik, S., and Cuervo, A.M. (2012). Chaperone-mediated autophagy: a unique way to enter the lysosome world. Trends Cell Biol. *22*, 407–417.

Kerkhoff, E., Simpson, J.C., Leberfinger, C.B., Otto, I.M., Doerks, T., Bork, P., Rapp, U.R., Raabe, T., and Pepperkok, R. (2001). The Spir actin organizers are involved in vesicle transport processes. Curr. Biol. *11*, 1963–1968.

Khuong, T.M., Habets, R.L., Kuenen, S., Witkowska, A., Kasprowicz, J., Swerts, J., Jahn, R., van den Bogaart, G., and Verstreken, P. (2013). Synaptic PI(3,4,5)P3 is required for Syntaxin1A clustering and neurotransmitter release. Neuron *77*, 1097–1108.

Kozlov, M.M., Campelo, F., Liska, N., Chernomordik, L.V., Marrink, S.J., and McMahon, H.T. (2014). Mechanisms shaping cell membranes. Curr. Opin. Cell Biol. *29*, 53–60.

Lloyd, T.E., Verstreken, P., Ostrin, E.J., Phillippi, A., Lichtarge, O., and Bellen, H.J. (2000). A genome-wide search for synaptic vesicle cycle proteins in Drosophila. Neuron *26*, 45–50.

Matta, S., Van Kolen, K., da Cunha, R., van den Bogaart, G., Mandemakers, W., Miskiewicz, K., De Bock, P.J., Morais, V.A., Vilain, S., Haddad, D., et al. (2012). LRRK2 controls an EndoA phosphorylation cycle in synaptic endocytosis. Neuron *75*, 1008–1021.

Morgan, J.R., Prasad, K., Jin, S., Augustine, G.J., and Lafer, E.M. (2001). Uncoating of clathrin-coated vesicles in presynaptic terminals: roles for Hsc70 and auxilin. Neuron *32*, 289–300.

Nosková, L., Stránecký, V., Hartmannová, H., Přistoupilová, A., Barešová, V., Ivánek, R., Hůlková, H., Jahnová, H., van der Zee, J., Staropoli, J.F., et al. (2011). Mutations in DNAJC5, encoding cysteine-string protein alpha, cause autosomal-dominant adult-onset neuronal ceroid lipofuscinosis. Am. J. Hum. Genet. *89*, 241–252.

Pak, W.L. (1995). Drosophila in vision research. The Friedenwald Lecture. Invest. Ophthalmol. Vis. Sci. *36*, 2340–2357.

Pandey, U.B., Nie, Z., Batlevi, Y., McCray, B.A., Ritson, G.P., Nedelsky, N.B., Schwartz, S.L., DiProspero, N.A., Knight, M.A., Schuldiner, O., et al. (2007). HDAC6 rescues neurodegeneration and provides an essential link between autophagy and the UPS. Nature *447*, 859–863.

Parton, R.G., and Simons, K. (2007). The multiple faces of caveolae. Nat. Rev. Mol. Cell Biol. *8*, 185–194.

Parzych, K.R., and Klionsky, D.J. (2014). An overview of autophagy: morphology, mechanism, and regulation. Antiox. Redox. Signal. *20*, 460–473.

Rogers, S., Wells, R., and Rechsteiner, M. (1986). Amino acid sequences common to rapidly degraded proteins: the PEST hypothesis. Science *234*, 364–368.

Sadis, S., and Hightower, L.E. (1992). Unfolded proteins stimulate molecular chaperone Hsc70 ATPase by accelerating ADP/ATP exchange. Biochemistry *31*, 9406–9412.

Sahu, R., Kaushik, S., Clement, C.C., Cannizzo, E.S., Scharf, B., Follenzi, A., Potolicchio, I., Nieves, E., Cuervo, A.M., and Santambrogio, L. (2011). Microautophagy of cytosolic proteins by late endosomes. Dev. Cell *20*, 131–139.

Sharma, M., Burré, J., and Südhof, T.C. (2011). CSPα promotes SNARE-complex assembly by chaperoning SNAP-25 during synaptic activity. Nat. Cell Biol. *13*, 30–39.

Shimazu, M., Sekito, T., Akiyama, K., Ohsumi, Y., and Kakinuma, Y. (2005). A family of basic amino acid transporters of the vacuolar membrane from Saccharomyces cerevisiae. J. Biol. Chem. *280*, 4851–4857.

Speese, S.D., Trotta, N., Rodesch, C.K., Aravamudan, B., and Broadie, K. (2003). The ubiquitin proteasome system acutely regulates presynaptic protein turnover and synaptic efficacy. Curr. Biol. *13*, 899–910.

Stachowiak, J.C., Schmid, E.M., Ryan, C.J., Ann, H.S., Sasaki, D.Y., Sherman, M.B., Geissler, P.L., Fletcher, D.A., and Hayden, C.C. (2012). Membrane bending by protein-protein crowding. Nat. Cell Biol. *14*, 944–949.

Subach, F.V., Subach, O.M., Gundorov, I.S., Morozova, K.S., Piatkevich, K.D., Cuervo, A.M., and Verkhusha, V.V. (2009). Monomeric fluorescent timers that change color from blue to red report on cellular trafficking. Nat. Chem. Biol. *5*, 118–126.

Sweitzer, S.M., and Hinshaw, J.E. (1998). Dynamin undergoes a GTP-dependent conformational change causing vesiculation. Cell *93*, 1021–1029.

Tobaben, S., Thakur, P., Fernández-Chacón, R., Südhof, T.C., Rettig, J., and Stahl, B. (2001). A trimeric protein complex functions as a synaptic chaperone machine. Neuron *31*, 987–999.

Uytterhoeven, V., Kuenen, S., Kasprowicz, J., Miskiewicz, K., and Verstreken, P. (2011). Loss of skywalker reveals synaptic endosomes as sorting stations for synaptic vesicle proteins. Cell *145*, 117–132.

Verstreken, P., Ohyama, T., and Bellen, H.J. (2008). FM 1-43 labeling of synaptic vesicle pools at the Drosophila neuromuscular junction. Methods Mol. Biol. *440*, 349–369.

Weir, M.P., and Rice, M.D. (2010). TRII: A Probabilistic Scoring of Drosophila melanogaster Translation Initiation Sites. EURASIP J. Bioinform. Syst. Biol. *2010*, 814127.

Wilhelm, B.G., Mandad, S., Truckenbrodt, S., Kröhnert, K., Schäfer, C., Rammner, B., Koo, S.J., Claßen, G.A., Krauss, M., Haucke, V., et al. (2014). Composition of isolated synaptic boutons reveals the amounts of vesicle trafficking proteins. Science *344*, 1023–1028.

Winter, U., Chen, X., and Fasshauer, D. (2009). A conserved membrane attachment site in alpha-SNAP facilitates N-ethylmaleimide-sensitive factor (NSF)-driven SNARE complex disassembly. J. Biol. Chem. *284*, 31817–31826.

Yao, I., Takagi, H., Ageta, H., Kahyo, T., Sato, S., Hatanaka, K., Fukuda, Y., Chiba, T., Morone, N., Yuasa, S., et al. (2007). SCRAPPER-dependent ubiquitination of active zone protein RIM1 regulates synaptic vesicle release. Cell *130*, 943–957.

Yu, C., Wan, K.H., Hammonds, A.S., Stapleton, M., Carlson, J.W., and Celniker, S.E. (2011). Development of expression-ready constructs for generation of proteomic libraries. Methods Mol. Biol. *723*, 257–272.

Zhai, R.G., Zhang, F., Hiesinger, P.R., Cao, Y., Haueter, C.M., and Bellen, H.J. (2008). NAD synthase NMNAT acts as a chaperone to protect against neurodegeneration. Nature *452*, 887–891.